JOURNAL OF SOLID STATE CHEMISTRY 117, 236–246 (1995)

Synthesis, Structure, and Properties of $Ln_4Ni_3O_{10-\delta}$ (Ln = La, Pr, and Nd)

Z. Zhang and M. Greenblatt[1]

Department of Chemistry, Rutgers—The State University of New Jersey, Piscataway, New Jersey 08855

Received June 27, 1994; in revised form November 29, 1994; accepted January 4, 1995

The Ruddlesden–Popper nickelates $Ln_4Ni_3O_{10-\delta}$, with Ln = La, Pr, and Nd, have been synthesized by a precursor method. Power X-ray diffraction studies show orthorhombic symmetry with space group *Fmmm* for all three compounds; however, electron diffraction patterns of single crystals show that the space group symmetry is lower than *F* or *C*. The orthorhombic unit cell parameters decrease monotonically with decreasing effective ionic radius of the lanthanide ion. The distortion from ideal tetragonal symmetry and the orthorhombic strain increase with decreasing radius of the lanthanide ion; Nd was the smallest lanthanide for which $Ln_4Ni_3O_{10-\delta}$ could be stabilized. $Pr_4Ni_3O_{10-\delta}$ and $Nd_4Ni_3O_{10-\delta}$ are oxygen deficient ($\delta \sim 0.15$), while $La_4Ni_3O_{10}$ is nearly stoichiometric. The resistivity measurements indicate metallic temperature dependence for $La_4Ni_3O_{10}$, and a metal-to-metal transition for $Pr_4Ni_3O_{10-\delta}$ and $Nd_4Ni_3O_{10-\delta}$ at 145 and 165 K, respectively. These anomalies are attributed to charge-density-wave driven instabilities and are confirmed by differential scanning calorimetry to coincide with first-order structural phase transitions. The magnetic susceptibility of metallic $La_4Ni_3O_{10}$ is nearly temperature independent above 100 K, and shows paramagnetic behavior at lower temperatures. $Pr_4Ni_3O_{10-\delta}$ and $Nd_4Ni_3O_{10-\delta}$ show paramagnetic behavior in the temperature range 4–300 K, due to the large magnetic contributions of the lanthanides to the total moment.

INTRODUCTION

The crystal structure of Ruddlesden–Popper (RP) phases can be described by the stacking of finite n layers of perovskite $LnNiO_3$ between rock salt LnO layers along the crystallographic c direction $((LnO)(LnNiO_3)_n$ (1). The corner-sharing NiO_6 octahedra form infinite sheets in the ab plane where strong electronic interactions can occur. With increasing n, anisotropic properties and an increase in dimensionality may be expected in RP phases. The first member of the RP family of nickelates, n = 1, is Ln_2NiO_4, which adopts the K_2NiF_4-type structure with only one layer of corner-sharing NiO_6 octahedra along the c direction. The symmetry of Ln_2NiO_4 can vary from tetragonal to orthorhombic depending on the nature of the lanthanide and the oxygen stoichiometry. Due to the typical two-dimensional (2D) structure and the oxidation state of nickel (near +2), all of the Ln_2NiO_4 compounds, if stoichiometric, show insulating properties at room temperature.

In the second member of the RP nickelates, $Ln_3Ni_2O_7$, two infinite NiO_6 sheets are connected in the c direction between the rock-salt layers. Since the nickel oxidation state and electronic correlations along the c direction increase relative to that of Ln_2NiO_4, the electrical conductivity is enhanced significantly. Recently, the relationship between the structure and properties of $La_3Ni_2O_{7-\delta}$ with different oxygen contents (δ = 0, 0.08, 0.16, and 0.35) has been reported (2). A semiconductor-to-metal transition was observed upon high-pressure oxygen annealing or divalent cation substitutions of the δ = 0.08 sample (3). The nearly temperature-independent Pauli-paramagnetic susceptibility seen in $La_3Ni_2O_{7-\delta}$ (with $\delta \leq 0.08$) at high temperature was attributed to partially delocalized electrons in a band of primarily metal 3*d*-oxygen 2*p* character. Anderson localization associated with oxygen defects was observed in the as-prepared $La_3Ni_2O_{6.92}$.

This work focused on the study of the n = 3 members, $Ln_4Ni_3O_{10-\delta}$, of the RP rare earth nickelates with Ln = La, Pr, and Nd. The structure of this family consists of infinite layers of perovskite-type $LnNiO_3$ with corner-sharing NiO_6 octahedra in the ab plane; three such layers are connected by corner-sharing along the c direction. The $(LnNiO_3)_3$ perovskite layers are separated by LnO rock-salt layers, as shown in Fig. 1. The synthesis of the first multilayered RP nickelates was reported by Wold and Arnott (4) in 1959, when they observed a phase with a La/Ni ratio between that of $LaNiO_3$ and La_2NiO_4. In 1979, Nakamura *et al.* identified an intermediate reduction product of $LaNiO_3$ as a member of the RP nickelates (5). Seppanen prepared $La_4Ni_3O_{10}$ successfully in 1979 and concluded that in the La–Ni–O system, $LaNiO_3$, La_2NiO_4, and $La_4Ni_3O_{10}$ were the only ternary compounds stable at elevated temperatures (6). Brisi *et al.* reported the powder X-ray diffraction data of $La_4Ni_3O_{10}$

[1] To whom correspondence should be addressed.

0022-4596/95 $12.00

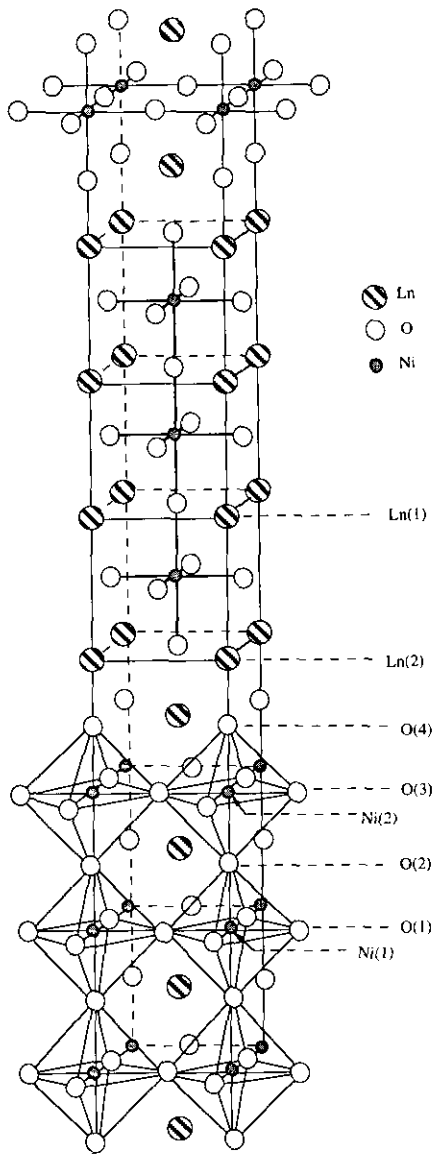

FIG. 1. The ideal crystal structure of $Ln_4Ni_3O_{10-\delta}$ showing a tetragonal unit cell.

for the first time in 1981 (7); however, their product, prepared by the decomposition of $LaNiO_3$, was not single phase. Further studies on $Ln_4Ni_3O_{10}$ were carried out by several groups, including Drennan *et al.* (8), Petrov *et al.* (9), Savhenko *et al.* (10), Mohan Ram *et al.* (11); Tkalich *et al.* (12), Sullivan and Buttrey (13), Lacorre (14), and Sreedhar *et al.* (15). Although the previous studies have provided new information on the RP nickelates with $n > 1$, the difficulties associated with the synthesis of monophasic specimens limited quantitative studies on their structural and physical properties.

The objectives of this study were: (i) to synthesize a series of single-phase $n = 3$ Ruddlesden–Popper nickelates, (ii) to systematically investigate the effect of the size of the lanthanide ion on the synthesis and properties, (iii) to investigate the effect of dimensionality of the RP nickelates on the properties, and (iv) to establish a more complete electronic band diagram across the homologous series of RP nickelates.

EXPERIMENTAL

Single-phase $Ln_4Ni_3O_{10}$, where Ln = La, Pr, and Nd, were prepared by a precursor method with different sintering conditions required for different rare earth elements.

All samples were made from starting materials NiO (Aldrich, 99.9%) and the corresponding lanthanides La_2O_3, Pr_6O_{11}, or Nd_2O_3 (Aldrich, 99.99%), which were preheated at 1000°C prior to use. The stoichiometric amounts of oxides were dissolved in 3 *M* nitric acid solution. A 25% aqueous solution of tetramethylammonium hydroxide was slowly added to this solution until a light-green precipitate formed. The solution containing the precipitate was gently heated on a hot plate to remove excess water and acid. The resulting solid was heated at about 350°C in a furnace to decompose the organic precursor. Thereafter the dark-gray product was ground to very fine powder and was cold-pressed into pellets (the pressure applied is about 1.8×10^4 psi).

Each precursor pellet was placed in a high-density alumina crucible and heat-treated as follows:

$La_4Ni_3O_{10}$ was calcined in the furnace at 1100°C for 4–5 days in air. Several (two to three times on average) intermittent grindings followed by repelletization were necessary to obtain single-phase $La_4Ni_2O_{10}$. The sample was furnace-cooled to 500°C and was annealed at this temperature for several hours in air; finally the sample was furnace-cooled to room temperature in air.

$Pr_4Ni_3O_{10-\delta}$ and $Nd_4Ni_3O_{10-\delta}$ were sintered in a tube furnace under 1 atm flowing oxygen at 1050 and 1000°C, respectively, for about 5–6 days for both samples. Several intermittent grindings (four to five times on average) followed by repelletization were necessary to diminish the amount of Nd_2O_3 and Pr_6O_{11}, respectively. The samples were furnace-cooled in flowing oxygen to 500°C and were annealed at this temperature under oxygen for several hours; finally, each sample was furnace-cooled under oxygen to room temperature.

The identity and purity of the samples were characterized by powder X-ray diffraction (PXD) on a SCINTAG PAD V diffractometer with CuK_α radiation. The observed PXD data were used for a least-squares refinement of the unit cell parameters. Mica was used as an internal standard for peak correction. The scan rate was 1° 2θ per min with chopper increments of 0.01° 2θ in the range $20° < 2\theta < 80°$.

The oxygen content was determined by thermogravimetric analysis (TGA) in a DuPont 951 thermogravimetric analyzer under a reducing atmosphere (flowing 10% H_2 in Ar). The heating rate was 2°C/min and the gas flowing rate was about 35 cm^3/min. The dc electrical resistivity of pressed pellets was measured with a standard four-probe technique in a closed-cycle cryostat (APD Cryogenics, DE 202) in the temperature range 20–300 K. The dc magnetic susceptibility measurements were carried out on a Quantum Design SQUID magnetometer (MPMS) in the temperature range 4–300 K in an applied magnetic field of 1000 G.

The homogeneity and defect character of the samples were examined by high-resolution electron microscopy (HREM) with a ISI-002B transmission electron microscope operating at 200 keV. Crystallites of $Nd_4Ni_3O_{10-\delta}$ were gently ground and dispered with alcohol on a porous carbon-coated copper grid. The grid was kept under mild vacuum to evaporate the solvent before the measurement. Thin crystals projecting through the holes of the grid were brought to the required orientation with the help of a goniometer. Selected area images and diffraction patterns were obtained for different crystallites. The images were recorded at a primary magnification of 4.9×10^5.

The differential scanning calorimetric (DSC) measurements have been carried out on a DuPont 910 differential scanning calorimeter. About 0.04 g of sample was loaded into an aluminum cap. To avoid any condensation of moisture during cooling, the sample was sealed between two caps by pressing. The system was cooled to about 100 K with liquid nitrogen and was slowly warmed to room temeprature at a heating rate of 5°C/min. Only the warming data were collected for the analysis.

RESULTS AND DISCUSSION

All three phases of $Ln_4Ni_3O_{10-\delta}$ are black; the Ln = La sample is single phase, while the Ln = Pr and Nd samples contain ~5% Pr_6O_{11} or Nd_2O_3 impurity, respectively.

1. Summary of the Synthetic Condition

The synthetic conditions determined empirically for selected RP nickelates are summarized in Table I.

It has been noted that with increasing number of perovskite layers ($LnNiO_3$) in $LnO(LnNiO_3)_n$, the sintering temperature required to stabilize the phase decreases. One of the factors affecting the temperature required for the formation of the RP nickelates appears to be the oxidation state of nickel. With increasing n, the nickel valence increases gradually from about +2 in Ln_2NiO_4 to +2.5 in $Ln_3Ni_2O_7$, +2.67 in $Ln_4Ni_3O_{10}$, and finally it reaches +3 in $LnNiO_3$. The high nickel valence can only be stabilized at lower temperature. For example, $LaNiO_3$ is only stable below 1000°C.

The sintering temperature required for the preparation of $Ln_4Ni_3O_{10-\delta}$ also decreased systematically with decreasing ionic radii across the lanthanide series. This behavior can be attributed to the increasing structural distortion with decreasing size of the lanthanide ion. Lower sintering temperature and longer sintering time help stabilize the more distorted metastable phases. The failure to synthesize $Ln_4Ni_3O_{10-\delta}$ with lanthanides smaller than Nd is consistent with the increasing instability of the structure with decreasing size of the lanthanide ion.

2. Structure

The powder X-ray diffraction patterns of all three samples can be indexed based on orthorhombic symmetry in space group *Fmmm* (Figs. 2a, 2b, and 2c). Some peak broadening was observed, especially at high 2θ angles, due to either a lowering of the crystal symmetry from *Fmmm* or poor crystallinity. The atomic positions of $La_4Ni_3O_{10}$, shown in Table 2, have been estimated from analogy with $Sr_4V_3O_{10}$ (16) with tetragonal to orthorhombic transformation without refinement. The calculated diffraction pattern of $Ln_4Ni_3O_{10-\delta}$ was generated with a "Lazy-Pulverix" program and is compared with experimental data in Table 3. The agreement between the calculated and observed relative reflection intensities for all three phases is in general satisfactory, considering that preferred orientation, temperature, and absorption factors were not taken into account in the calculations.

The unit cell parameters, determined from a least-squares refinement of the PXD data, are listed in Table 4 and illustrated in Figs. 3a and 3b. The cell parameters of $Ln_4Ni_3O_{10-\delta}$ are generally in good agreement with those previously reported in the literature (12, 14, 15). From La

TABLE 1
Summary of the Synthetic Conditions of Selected RP Phases

	La_2NiO_4	$La_3Ni_2O_7$	$La_4Ni_3O_{10}$	$Pr_4Ni_3O_{10}$	$Nd_4Ni_3O_{10}$	$LaNiO_3$
Temperature (°C)	1200	1150	1100	1050	1000	800
Time (days)	2–3	4–5	4–5	5–6	5–6	8–10 hr
Atmosphere	Air	Air	Air	Flowing O_2	Flowing O_2	Flowing O_2

TABLE 2
Atomic Positions of La, Ni, and O in $La_4Ni_3O_{10}$ (Space Group *Fmmm*) after Ref. (16)

Atom	Position	x	y	z
La(1)	8*i*	0	0	0.431
La(2)	8*i*	0	0	0.298
Ni(1)	4*a*	0	0	0
Ni(2)	8*i*	0	0	0.139
O(1)	8*e*	1/4	1/4	0
O(2)	8*i*	0	0	0.07
O(3)	16*j*	1/4	1/4	0.14
O(4)	8*i*	0	0	0.21

to Nd, all three unit cell parameters decrease monotonically with decreasing ionic radii of the lanthanides, demonstrating that the unit cell parameters are affected only by the effective size of the *Ln* ions. The decrease in the a parameter is larger than that in the b parameter; therefore the orthorhombic strain, expressed by the equation $s = 2(b - a)/(b + a)$, increases from $La_4Ni_3O_{10}$ to $Nd_4Ni_3O_{10-\delta}$, due to the decrease in the ionic radii of the lanthanides. This effect has been seen by Lavrova *et al.* (17) as well, who observed an orthorhombic to tetragonal phase transition in $La_4Ni_3O_{10}$ at 985 K.

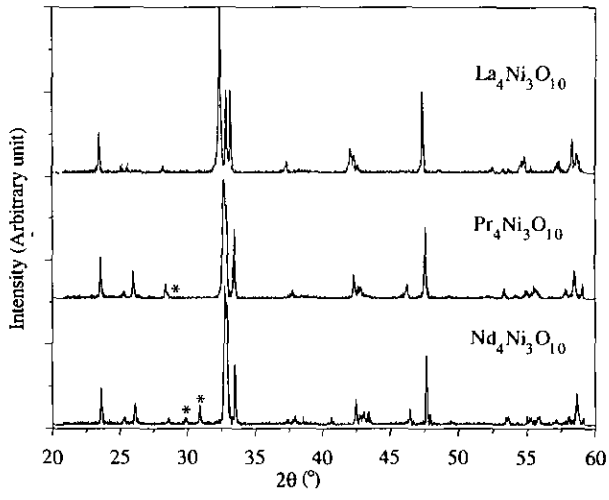

FIG. 2. The X-ray pattern of $La_4Ni_3O_{10}$, $Pr_4Ni_3O_{10-\delta}$, and $Nd_4Ni_3O_{10-\delta}$. (The asterisks indicate Nd_2O_3 and Pr_6O_{11} impurities).

The total decrease in the c parameter from the La to the Nd compound is 0.56 Å, which is much larger than the decreases in the a and b parameters: 0.053 and 0.013 Å, respectively. This can be attributed to the cumulative effect of reduced lanthanide radii along the c direction where the layers are stacked.

TABLE 3
Experimental and Calculated PXD Data in $Ln_4Ni_3O_{10-\delta}$ in Space Group *Fmmm*[a]

			$La_4Ni_3O_{10-\delta}$		$Pr_4Ni_3O_{10-\delta}$		$Nd_4Ni_3O_{10-\delta}$			
h	k	l	d_{obs}	d_{calc}	d_{obs}	d_{calc}	d_{obs}	d_{calc}	I_{obs}[b]	I_{calc}
1	1	1	3.813	3.811	3.793	3.793	3.782	3.786	23	12
1	1	3	3.554	3.556	3.537	3.534	3.530	3.526	6	2
0	0	8	3.493	3.495	3.442	3.441	3.424	3.426	11	6
1	1	7	2.772	2.771	2.743	2.743	2.735	2.735	100	100
0	2	0	2.733	2.734	—	2.731	2.723	2.725	49	28
2	0	0	2.708	2.708	2.684	2.685	2.680	2.681	48	27
1	1	9	—[c]	2.417	2.386	2.389	2.377	2.382	2	1
0	2	8	2.152	2.153	2.140	2.139	2.133	2.133	18	9
2	0	8	2.141	2.141	—	2.117	2.116	2.111	9	9
0	0	14	1.996	1.997	1.967	1.966	1.959	1.958	12	14
2	2	0	1.923	1.923	1.915	1.915	1.911	1.911	49	31
1	3	1	—	1.723	1.721	1.721	1.718	1.719	2	2
1	1	15	1.678	1.678	1.653	1.655	1.650	1.649	7	4
0	2	14	1.611	1.612	1.596	1.596	1.591	1.590	6	8
2	0	14	1.607	1.607	—	1.586	—	1.581	7	8
1	3	7	1.585	1.585	1.5578	1.579	1.576	1.576	21	17
3	1	7	1.574	1.575	1.562	1.561	1.555	1.558	10	16
2	2	14	1.385	1.385	1.373	1.372	—	1.367	3	2
0	4	0	1.365	1.366	1.365	1.365	1.364	1.363	4	4
4	0	0	1.354	1.354	1.343	1.343	1.341	1.341	2	4

[a] The error in the d values is ±0.001.
[b] The differences between experimental and calculated relative intensities for different lanthanides are negligible.
[c] Not observed or not resolved experimentally.

TABLE 4
The Cell Parameters, Oxygen Content, Orthorhombic Strain, and Tolerance Factor of $Ln_4Ni_3O_{10-\delta}$

	a (Å)	b (Å)	c (Å)	V (Å)^3	s^a	t^b	ρ_{RT} (Ω-cm)
$La_4Ni_3O_{10.0}$	5.415(1)	5.465(1)	27.959(9)	827.4(3)	9.19×10^{-3}	0.932	5×10^{-3}
$Pr_4Ni_3O_{9.85}$	5.370(1)	5.462(1)	27.528(7)	807.3(2)	1.69×10^{-2}	0.917	1×10^{-2}
$Nd_4Ni_3O_{9.85}$	5.362(1)	5.454(1)	27.410(6)	801.0(3)	1.73×10^{-2}	0.910	5×10^{-2}

[a] Orthorhombic strain, $s = 2(b - a)/(b + a)$.
[b] Tolerance factor, $t = (r_{Ln} + r_O)/\sqrt{2}(r_{Ni} + r_O)$.

It is well known that the stability of the perovskite-type structure can be described by a tolerance factor, which is defined in the case of nickelates as

$$t = (r_{Ln} + r_O)/\sqrt{2}(r_{Ni} + r_O). \quad [1]$$

This relationship is based on packing considerations and is a relevant parameter for estimating the degree of distortion of the tetragonal unit cell when no other effects are involved. The ideal value of t is 1 and the tetragonal-to-orthorhombic distortion increases with decreasing t. The t values of $Ln_4Ni_3O_{10-\delta}$, calculated from the ionic radii of Shannon (18), are listed in Table 4; t decreases systematically with decreasing radii of lanthanides. This trend is indicative of a systematic increase in distortion from ideal tetragonal symmetry and its consequences were discussed regarding the trends in the synthetic conditions.

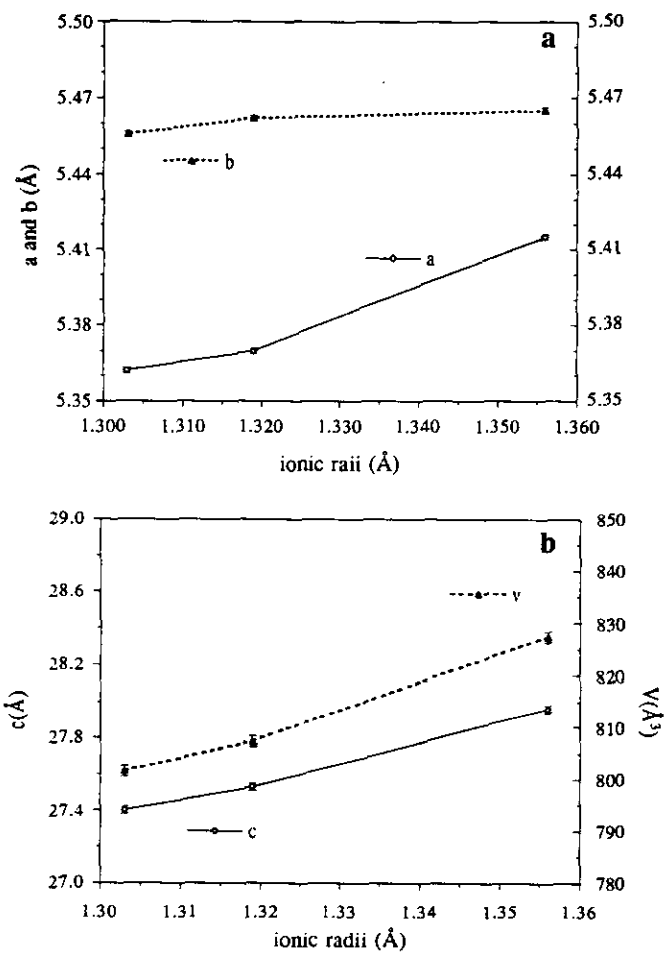

FIG. 3. The variation in the unit cell parameters of $Ln_4Ni_3O_{10-\delta}$ versus ionic radius of the lanthanides. (a) a and b parameters; and (b) c and V parameters.

In comparison with the other members of the series, the interpretation of the unit cell dimensions of $Pr_4Ni_3O_{10-\delta}$ is complicated by the two possible valence states of praseodymium (+3 and +4). If a significant amount of Pr^{4+} is present in the phase, both the c parameter and the tolerance factor would be considerably reduced. However, the c parameter lies on the same curve as the c parameters for the other two lanthanide compounds, and similar patterns are seen for the trends in the synthetic conditions and the metal-to-semiconductor transition temperature (see Discussion). Therefore, we believe that in $Pr_4Ni_3O_{10-\delta}$ praseodymium is primarily in the +3 oxidation state.

3. Oxygen Content

The total oxygen content of each sample was determined by TGA measurement with Ln_2O_3 and Ni as final products as evidenced by PXD (even in the case of the praseodymium compound, where Pr_6O_{11} was used as the starting material). The results of oxygen analysis are presented in Table 4 along with the unit cell parameters. A common feature of the reduction curves of $Ln_4Ni_3O_{10-\delta}$ was a two-step behavior illustrated in Fig. 4. For the Pr and Nd compounds, the first plateau seen in the temperature range 450–550°C is associated with the stabilization of an intermediate phase corresponding to the approximate compositions: $Pr_4Ni_3O_8$ and $Nd_4Ni_3O_8$. The corresponding intermediate phase of $La_4Ni_3O_{10}$ has the approximate composition $La_4Ni_3O_9$. However, under a pure H_2 atmosphere, Lacorre obtained $La_4Ni_3O_8$ (14). It is not clear why the same reducing conditions lead to different products for different lanthanides. The second

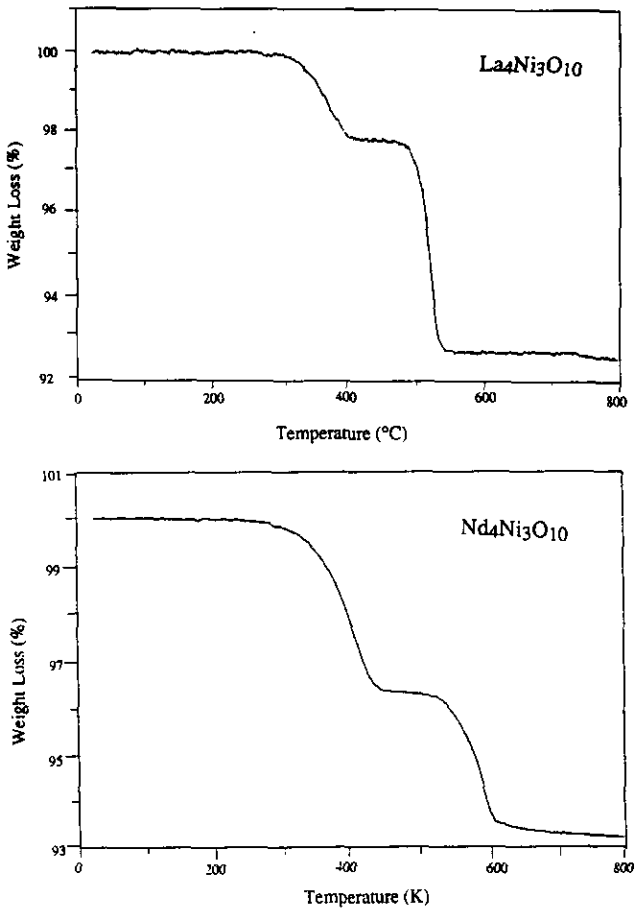

FIG. 4. The TGA (weight loss) of $La_4Ni_3O_{10}$ and $Nd_4Ni_3O_{10-\delta}$.

weight loss above 600°C for all three samples is associated with the decomposition of the compounds.

The oxygen content was determined from the total weight loss. Significant oxygen deficiency was observed in the Nd and Pr compounds whereas the La compound is nearly oxygen stoichiometric. The observed oxygen deficiency for the Nd and Pr compounds could be partially due to the presence of some starting materials in these samples. Although an oxygen deficiency was observed in as-prepared $La_3Ni_2O_{6.92}$, as-prepared $La_4Ni_3O_{10}$ is stoichiometric. The fact that $Nd_3Ni_2O_7$ and $Pr_3Ni_2O_7$ cannot be prepared under similar conditions as those for $Nd_4Ni_3O_{10-\delta}$ and $Pr_4Ni_3O_{10-\delta}$ indicates differences in stability across the homologous series of RP nickelates.

It has been noted that the thermodynamically stable phases of $La_2NiO_{4+\delta}$ and $Nd_2NiO_{4+\delta}$ form with excess oxygen, while higher members of RP phases usually display oxygen deficiency (19). Incorporation of excess oxygen is required to stabilize the structure of compounds containing nickel only in the +2 state (i.e., La_2NiO_4); the excess oxygen leads to mixed valency in the NiO_2 planes (20) and a higher tolerance factor (Eq. [1]). However, electronic effects may also be operating to optimize the stability of the RP phases. For any of the $1 < n < \infty$ members of the RP phases, the compounds always have mixed valency of nickel and therefore either oxygen stoichiometry (e.g., $La_4Ni_3O_{10}$) or oxygen deficiency (e.g., $Nd_4Ni_3O_{10-\delta}$ and $Pr_4Ni_3O_{10-\delta}$) is possible.

4. Transmission Electron Microscope

A high-resolution electron microscopic study was carried out on $Nd_4Ni_3O_{10-\delta}$ to confirm the identity of the phase from powder X-ray results and to examine the microstructure including homogeneity, phase ordering, and the extent of defects or intergrowth.

The sharp and clear HREM images and electron diffraction patterns show the high quality and crystallinity of the microcrystallites. Since the color contrast in the HREM image is sensitive to the imaging conditions, the assignment of contrasts to atoms will be different when the focus of the microscope or the thickness of the crystal is changed. A typical HREM image, shown in Fig. 5a, displays an array of broad zones separated by dark valleys (the view plane is either (010) or (100)). Each broad zone, corresponding to a perovskite lamella, contains four layers of bright dots and three layers of gray dots. The bright dots correspond to the position of neodymium atoms while the gray ones correspond to the position of nickel atoms. Therefore, each unit cell is composed of two perovskite lamellae in the c direction and two Nd (or

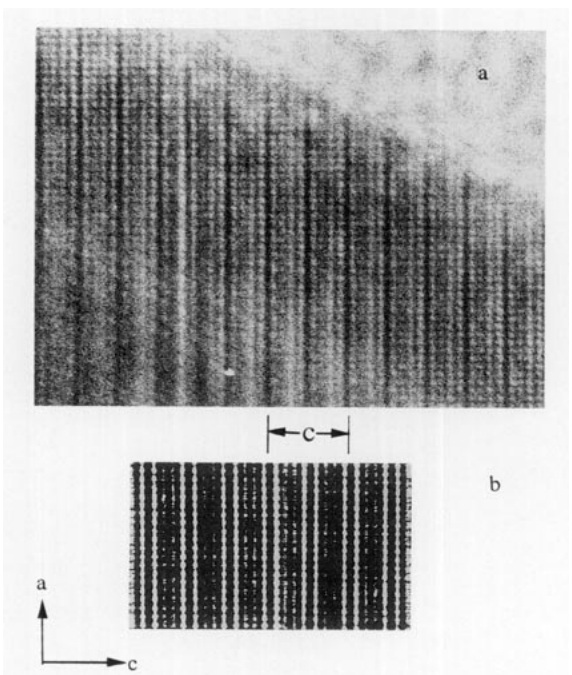

FIG. 5. The HREM image of $Nd_4Ni_3O_{10-\delta}$ along the [010] direction. (a) Experimental image; and (b) computer simulated image.

Ni) dots along the a or b direction. The atomic coordinates and the cell parameters obtained from PXD were used to simulate a calculated image in Fig. 5b, which is in good agreement with that obtained experimentally. The interpretation of the experimental image is also consistent with the two-dimensional projection of the schematic structure shown in Fig. 6.

The disordered intergrowths of different n members of RP phases have been reported in previous studies (11). However, we did not see a significant amount of disordered intergrowth or superstructure in our samples. After careful searching, one defect corresponding to "$Nd_3Ni_2O_7$," indicated with an asterisk in Fig. 5a, was observed. Since the quantity of the intergrowth is negligible, we would expect the properties of the compound to reflect the features of the nominal composition (i.e., $Nd_4Ni_3O_{10-\delta}$). A similar absence of intergrowth or defects was also observed by Sreedhar *et al.* in the HREM of $La_4Ni_3O_{10}$ (15).

The orientation of the crystallite in the electron diffraction measurements is along the [010] direction as determined from c/a and c/b considerations. The major bright reflections of electron diffraction patterns in Fig. 7 from 000 along the c^* direction can be indexed as 002, 004, 006, . . . , 00l, where $l = 2n$. The bright reflections in the next row can be indexed as 200, 202, 204, 206, . . . , 20l, where h, $l = 2n$. The relatively weaker reflections in a row between two major rows can be indexed as 101, 103, 105, . . . , 10l, or 301, 303, 305, . . . , 30l, where $h + l = 2n$. These reflections are forbidden in *Fmmm* and suggest that the space group symmetry is lower. We have attempted to observe some of these reflections by powder X-ray diffraction, but failed to see even the strongest ones by very slow 2θ scan. Tkalish *et al.* reported space group *Cmca* based on Rietveld analysis of their powder neutron diffraction data (12) on impure samples of $Ln_4Ni_3O_{10}$ (Ln = La, Pr, Nd). However, the h 0l reflections seen in our TEM (i.e., h, $l \neq 2n$; $h + l = 2n$) violate the space group extinction rules for *Cmca* as well. Thus the highest possible symmetry space group allowed is *Imm*2. Either single crystal X-ray analysis or more detailed powder data are required to resolve the symmetry of these phases.

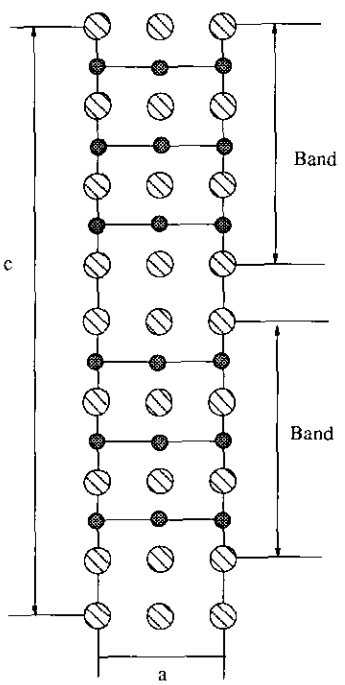

FIG. 6. The schematic projection of $Nd_4Ni_3O_{10-\delta}$ along the [010] direction.

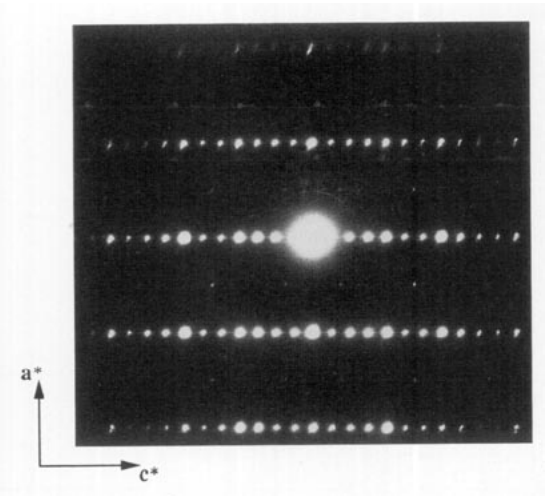

FIG. 7. The electron diffraction pattern of $Nd_4Ni_3O_{10-\delta}$ in the a^*c^* plane.

5. *Electrical Resistivity*

One of the most interesting physical properties of the RP nickelates is their electrical conductivity. The temperature (T) dependence of the resistivity (ρ) of $Ln_4Ni_3O_{10-\delta}$ samples is illustrated in Fig. 8. $La_4Ni_3O_{10}$ is one of the very few oxides that exhibit metallic conductivity even at very low temperature. The room temperature resistivity ρ_{RT} of $La_4Ni_3O_{10}$ is about 5×10^{-3} Ω-cm, two to three orders of magnitude larger than that of a normal metal and comparable to values reported earlier (11, 12, 15). The ρ vs T of $La_4Ni_3O_{10}$ is more linear in the high-temperature region than in the low-temperature region (Fig. 8).

Near room temperature, the resistivities of the $Pr_4Ni_3O_{10-\delta}$ and $Nd_4Ni_3O_{10-\delta}$ are progressively higher than that of $La_4Ni_3O_{10}$, but show metallic behavior of temperature dependence. $Pr_4Ni_3O_{10-\delta}$ and $Nd_4Ni_3O_{10-\delta}$ exhibit metal-to-metal transitions at about 145 and 165 K, respectively

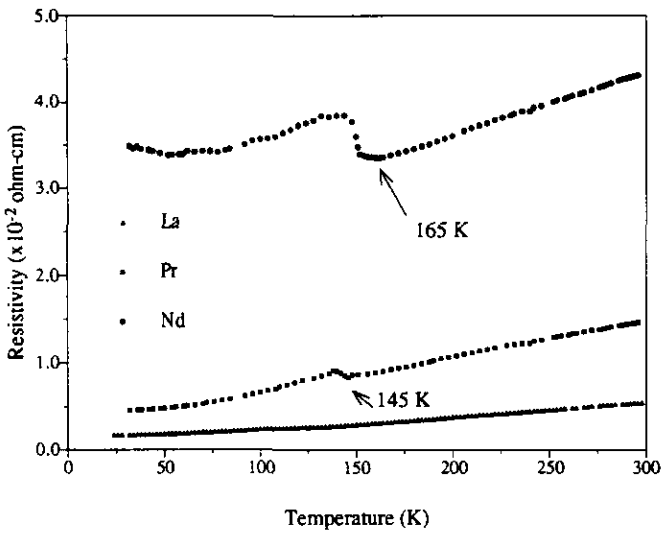

FIG. 8. The temperature dependence of the resistivity of $La_4Ni_3O_{10}$, $Pr_4Ni_3O_{10-\delta}$, and $Nd_4Ni_3O_{10-\delta}$.

(see Fig. 8). The anomalies seen in the resistivities of $Pr_4Ni_3O_{10-\delta}$ and $Nd_4Ni_3O_{10-\delta}$ were also observed by Tkalich *et al.* (12) and are likely associated with a first-order structural transition, since a small hysteresis is observed in the resistivity measurements of both near the transition. For the same member of the RP phase (i.e., same n in $(LnO)(LnNiO_3)_n$), the increase in the room temperature resistivity and the increase in the transition temperature with decreasing ionic radii of lanthanide ion demonstrate the effect of ionic radii on the structure and the transport properties.

As the effective ionic radius of the lanthanide decreases in $(LnO)(LnNiO_3)_n$, the tolerance factor decreases, and the structural distortion from ideal perovskite is enhanced. Since the layers of corner-sharing NiO_6 octahedra have a dominant effect on the electrical conductivity, electron localization could be significantly enhanced due to the increased structural distortion. The dramatic change in the ρ_{RT}, the anomalies in the resistivity, and the structural transitions in the $Ln_4Ni_3O_{10-\delta}$ (Ln = Pr, Nd) phases could be due to several factors: (i) a change in the Ni–O distances, and/or (ii) a sudden increase in the tilt of the NiO_6 octahedra, a decrease of Ni–O–Ni angle, and consequently a change in the Ni–O–Ni overlap.

The $Ln_4Ni_3O_{10-\delta}$ phases are quasi-two-dimensional materials susceptible to a Peierls transition or charge-density-wave (CDW) instability at a critical temperature. There is no evidence of CDW in the La compound in Fig. 8, but Tkalich *et al.* observed an anomaly at 150 K (12); moreover, the shape of ρ vs T at the transition of the Pr and Nd phases at 440 and 165 K, respectively, are typical of those seen in two-dimensional CDW compounds (21). Therefore, the transitions observed in the Pr and Nd phases are tentatively ascribed to CDW-driven instabilities. The dimensionality should increase with increasing Ln radius, consistent with the decreasing T_c from Nd > Pr. The first-order structural transition, as confirmed by the DSC, accompanying the partial opening of a gap at the Fermi surface is consistent with a CDW transition (22). Unambiguous evidence of CDW in these phases of course requires the observation of superlattice lines by diffraction methods. Such measurements must await the availability of single crystals of these phases.

It is noteworthy that for $PrNiO_3$ and $NdNiO_3$ with 3D perovskite structure, the ρ vs T data indicate a metal-to-insulator transition which was attributed to an electronically induced localization effect (23). In the 3D perovskite materials the electronic correlations are dramatically different from those we observe in the quasi-two-dimensional-RP phases here.

6. *Electronic Band Structure*

Across the homologous series of RP phases, the oxidation state of nickel and the dimensionality of the structure increase gradually. In La_2NiO_4, nickel has a formal valence of +2, which should present metallic behavior due to a half-filled e_g band. However, La_2NiO_4 is insulating, due to strong electronic correlations and short-range magnetic interactions that split the doubly occupied $\sigma^*_{x^2-y^2}$ and $d^*_{z^2}$ bands into two singly occupied bands (24). With increasing T, the energy gap between the $\sigma^{*1}_{x^2-y^2}$ and $\sigma^{*2}_{x^2-y^2}$ bands decreases and finally vanishes, and metallic properties are observed (T > 500 K for La_2NiO_4). Upon oxidation of RP nickelates, electrons are first gradually removed from the $\sigma^*_{x^2-y^2}$ band, which is at a higher energy level than the $d^*_{z^2}$ band. This analysis is supported by the change in the unit cell parameters with the substitution of Sr for Ln in $Ln_{2-x}Sr_xNiO_4$ (19, 25) and by the fact that the bond distance of Ni–O ($\|c$) is longer than that of Ni–O ($\perp c$) in Ln_2NiO_4. With an increase in hole content in the itinerant $\sigma^*_{x^2-y^2}$ band, the conductivity was expected to increase, as was observed in semiconducting $Ln_{2-x}Sr_xNiO_4$ with an increase in x (19, 25).

The change in the unit cell parameters in $Ln_{2-x}Sr_xNiO_4$ with increasing x (19, 25), as well as those of $La_{3-x}M_xNi_2O_{7-\delta}$ (M = Ca, Sr, and Ba, $0 < x < 0.075$) (3) by oxygenation, indicate a crossover of electronic configuration at a critical composition for these systems (i.e., $d^*_{z^2}$ is above $\sigma^*_{x^2-y^2}$ at $x > 0.5$ in $Nd_{2-x}Sr_xNiO_4$).

The c cell parameter increases by 7.437(1) Å from $La_3Ni_2O_7$ to $La_4Ni_3O_{10}$, mainly due to the four additional Ni–O bonds per unit cell along the c direction. If the average Ni–O bond length along the c direction is about 1.97 Å, four Ni–O bonds should be about 7.88 Å, which is much larger than the observed difference in the c parame-

ters between $La_3Ni_2O_7$ and $La_4Ni_3O_{10}$. Thus it is reasonable to assume that the hybridization of the nickel $3d$ and oxygen $2p$ orbitals along the c direction increases significantly with increasing nickel formal valence and increasing 3D character of the perovskite layers. Consequently, the narrow d_z^{*2} band in Ln_2NiO_4 with localized electrons is much broader in $La_3Ni_2O_7$ and even broader in $La_4Ni_3O_{10}$. With an extension of the electronic correlations along the c direction, the electrons are increasingly delocalized in the e_g bands. Figure 9 shows a schematic band diagram of $La_4Ni_3O_{10}$, in comparison with that of $La_3Ni_2O_7$ and La_2NiO_4. The significantly lower ρ_{RT} ($\sim 5 \times 10^{-3}$ Ω-cm) of $La_4Ni_3O_{10}$ compared to that of $La_3Ni_2O_7$ ($\sim 10^{-2}$ Ω-cm) and the semiconducting behavior La_2NiO_4 at room temperature is consistent with the band diagram shown in Fig. 9.

7. *Differential Scanning Calorimetry*

The observed transitions in the resistivity of the $Pr_4Ni_3O_{10-\delta}$ and $Nd_4Ni_3O_{10-\delta}$ phases could be attributed to various effects. To further investigate the origin of the anomalies, a DSC measurement was carried out from 100 K to room temperature. The endothermic peaks (Fig. 10) observed at about 145 and 165 K for $Pr_4Ni_3O_{10-\delta}$ and $Nd_4Ni_3O_{10-\delta}$, respectively, are consistent with the metal-to-metal transition seen in the resistivity measurements. The structural phase transition coincides with the metal-to-metal transition driven most likely by structural distortions or electronic instability or both, which generate a partial opening of a gap at the Fermi surface.

8. *Magnetic Susceptibility*

The variations of the magnetic susceptibility with temperature in $Ln_4Ni_3O_{10-\delta}$ is illustrated in Fig. 11. The results of $La_4Ni_3O_{10}$ are the simplest to interpret, since lanthanum is diamagnetic. At high temperature (100–300 K), the susceptibility has a weak temperature-dependent, nearly Pauli-paramagnetic behavior due to electron delocalization resulting from the strong Ni–O–Ni orbital overlap. The magnetic properties are consistent with the metallic behavior seen in the electrical resistivity measurements and are the same as those reported in Refs. (11) and (15).

However, the molar susceptibility is anomalously high ($\sim 1 \times 10^{-3}$ emu/mole; more than an order of magnitude greater than that expected for a free-electron model). The high value of susceptibility in perovskite-type nickelates was attributed by Goodenough *et al.* (26) to a Stoner-type enhancement, due to high ferromagnetic correlations of electrons in a quarter-filled e_g band associated with Ni^{3+} ions in $3d^7$ configuration (27). The weak temperature dependence of susceptibility indicates that short-range antiferro/ferromagnetic interactions of the type Ni^{2+}–O–Ni^{2+}/Ni^{2+}–O–Ni^{3+} are present. No long-range magnetic ordering was observed in any of the $Ln_4Ni_3O_{10-\delta}$ phases studied here. The upturn of susceptibility at low tempera-

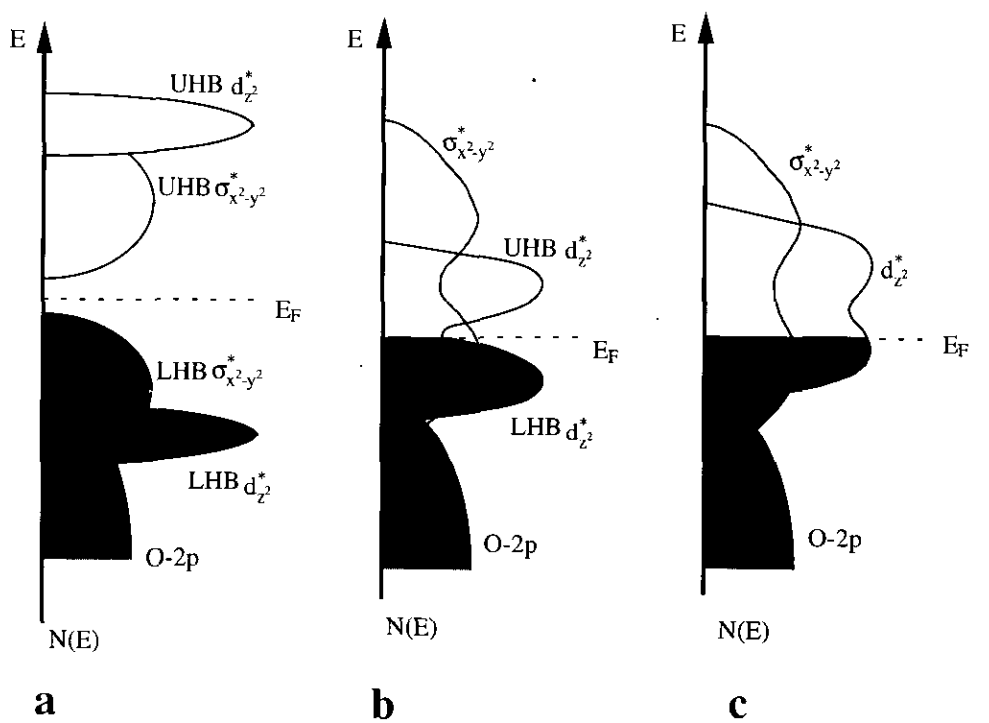

FIG. 9. The schematic diagram of density of states near the Fermi energy E_F of: (a) La_2NiO_4, (b) $La_3Ni_2O_7$; and (c) $La_4Ni_3O_{10}$.

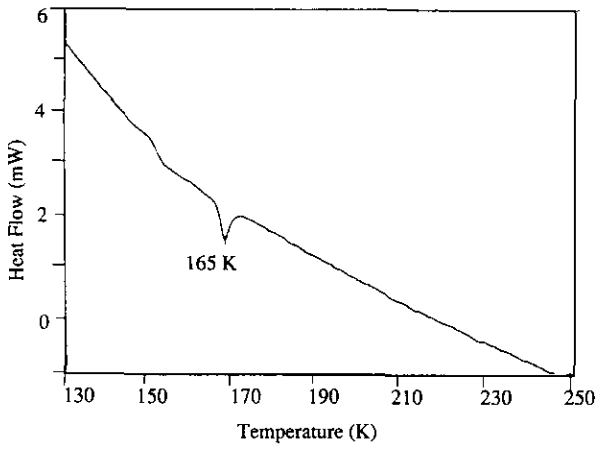

FIG. 10. The DSC curve of $Nd_4Ni_3O_{10-\delta}$.

ture suggests that magnetic impurities may be present in the system.

The susceptibility data of $Pr_4Ni_3O_{10-\delta}$ and $Nd_4Ni_3O_{10-\delta}$ are more complicated due to the large contribution of the local paramagnetic moment from Pr or Nd, which may mask small temperature-dependent variations in the susceptibility values.

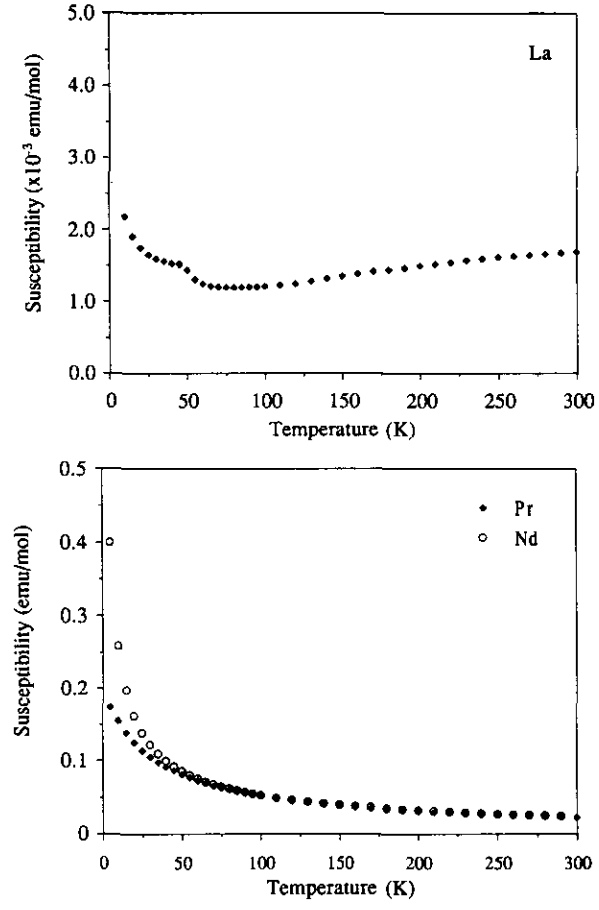

FIG. 11. The temperature dependence of the magnetic susceptibility of $La_4Ni_3O_{10}$, $Pr_4Ni_3O_{10-\delta}$, and $Nd_4Ni_3O_{10-\delta}$ (the small anomaly seen in the susceptibility of $La_4Ni_3O_{10-\delta}$ at ~50 K is due to adsorbed O_2).

CONCLUSIONS

A series of Ruddlesden–Popper nickelates, $Ln_4Ni_3O_{10-\delta}$ with Ln = La, Pr, and Nd, was synthesized by a precursor method. The powder X-ray diffraction data show orthorhombic symmetry with space group *Fmmm* for each. The cell parameters along all three directions decrease from La to Nd, consistent with the decrease in the ionic radii of lanthanide. The size effect of the lanthanide ions on the structure can be accounted for by the decrease in the tolerance factor and the increase in orthorhombic strain with decrease in lanthanide size.

The oxygen content analysis shows a small oxygen deficiency in the Pr and Nd compounds and near oxygen stoichiometry in the La analog. The high-resolution electron microscopic investigation of $Nd_4Ni_3O_{10-\delta}$ confirmed the stoichiometry of the sample and the structural data obtained from powder X-ray diffraction. However, the electron diffraction patterns of single crystals show that the orthorhombic space group symmetry is lower than *F* or *C*. The absence of significant structural disorder or intergrowth supports the interpretation of the structural and physical properties.

The resistivity measurements indicate metallic temperature dependence for all $Ln_4Ni_3O_{10-\delta}$; a metal-to-metal transition is observed for Ln = Pr and Nd at 145 and 165 K, respectively. These anomalies are attributed to CDW-driven instabilities. DSC measurements indicate that the anomalies seen in the resistivity are associated with a first-order structural transition, consistent with a CDW instability. The increasing trend in the transition temperature correlates well with the ionic radii of the lanthanides.

The magnetic susceptibility of $La_4Ni_3O_{10}$ is nearly temperature independent at high temperature, consistent with the metallic property; a paramagnetic upturn at low temperature is indicative of low-level paramagnetic impurities. Due to the large magnetic moment of Nd and Pr, the susceptibility of nickel ions is completely masked in $Nd_4Ni_3O_{10-\delta}$ and $Pr_4Ni_3O_{10-\delta}$.

ACKNOWLEDGMENTS

The authors thank Drs. W. H. McCarroll, K. V. Ramanujachary, and S. C. Chen for useful discussions. The HREM study was carried out in the Ceramics Department of Rutgers University with the help of Dr. P. Lu and Ms. M. Roepcke. This research was supported by National Science Foundation Solid State Chemistry Grants DMR-90-19301 and DMR-93-14605.

REFERENCES

1. S. N. Ruddlesden and P. Popper, *Acta Crystallogr.* **11,** 54 (1958).
2. Z. Zhang, M. Greenblatt, and J. B. Goodenough, *J. Solid State Chem.* **108,** 402 (1994).
3. Z. Zhang and M. Greenblatt, *J. Solid State Chem.* **111,** 141 (1994).
4. A. Wold and R. J. Arnott, *J. Phys. Chem. Solids* **9,** 1959 (1959).
5. T. Nakamura, G. Petzow, and L. J. Gauckel, *Mater. Res. Bull.* **14,** 649 (1979).
6. M. Seppanen, *Scand. J. Metall.* **8,** 1979 (1979).
7. C. Brisi, M. Vallino, and F. Abbattista, *J. Less-Common Met.* **79,** 215 (1981).
8. J. Drennan, C. P. Tavares, and B. C. H. Steele, *Mater. Res. Bull.* **17,** 621 (1982).
9. A. N. Petrov, V. A. Cherepanow, A. Y. Zuyev, and V. M. Zhukovsky, *J. Solid State Chem.* **77,** 1 (1988).
10. V. F. Savhenko, L. S. Ivashkevich, and I. Y. Lyubkina, *Russ. J. Inorg. Chem. Engl. Transl.* **33,** 17 (1988).
11. R. A. Mohan Ram, L. Ganapathi, P. Ganguly, and C. N. R. Rao, *J. Solid State Chem.* **63,** 139 (1986).
12. A. K. Tkalich, V. P. Glazkov, V. A. Somenkov, and S. S. Shil'shtein, *Superconductivity* **4**(12), 2281 (1992).
13. J. D. Sullivan and D. J. Buttrey, *J. Solid State Chem.* **94,** 337 (1991).
14. P. Lacorre, *J. Solid State Chem.* **97,** 495 (1992).
15. K. Sreedhar, M. McElfresh, D. Perry, K. Kim, P. Metcalf, and J. M. Honig, *J. Solid State Chem.* **110,** 208 (1994).
16. N. Ohashi, Y. Teramoto, H. Ikawa, O. Fukunaga, and J. Tanaka, *J. Solid State Chem.* **97,** 434 (1992).
17. O. A. Lavrova, V. A. Somenkov, A. K. Tkalich, and S. S. Shul'shtein, *Superconductivity* **4**(10), 1743 (1991).
18. R. D. Shannon, *Acta Crystallogr. Sect. A.* **32,** 751 (1976).
19. B. Arbuckle, K. V. Ramanujachary, Z. Zhang, and M. Greenblatt, *J. Solid State Chem.* **88,** 278 (1990).
20. S. C. Chen, K. V. Ramanujachary, and M. Greenblatt, *J. Solid State Chem.* **105,** 444 (1993).
21. M. Greenblatt, *Int. J. Mod. Phys. B* **7**(23/24), 3937 (1993).
22. P. A. Cox, "The Electronic Structure and Chemistry of Solids," Chap. 6. Oxford Univ. Press, London, 1987.
23. J. L. Garcia-Munoz, J. Rodriguez-Carvajal, P. Lacorre, and J. B. Torrance, *Phys. Rev. B* **46,** 4414 (1992).
24. J. B. Goodenough and S. Ramasesha, *Mater. Res. Bull.* **17,** 383 (1982).
25. J. Gopalakrishnan, G. Colsmann, and B. Reuter, *J. Solid State Chem.* **22,** 145 (1977).
26. J. B. Goodenough, N. F. Mott, M. Pouchard, G. Demazeau, and P. Hagenmuller, *Mater. Res. Bull.* **8,** 647 (1973).
27. J. B. Goodenough, *in* "Progress in Solid State Chemistry," p. 145. Pergamon, Elmsford, NY, 1971.